ELSEVIER

Journal of Alloys and Compounds 452 (2008) 210–216

Journal of ALLOYS AND COMPOUNDS

www.elsevier.com/locate/jallcom

Ferromagnetic properties of Ce_7Rh_3 and Pr_7Rh_3 single crystals

Takanori Tsutaoka [a,*], Yuko Nakamori [b]

[a] *Graduate School of Education, Hiroshima University, Higashi-Hiroshima 739-8524, Japan*
[b] *Institute for Materials Research, Tohoku University, Katahira, Aoba-ku, Sendai 980-8577, Japan*

Received 5 October 2006; received in revised form 2 November 2006; accepted 6 November 2006
Available online 6 December 2006

Abstract

Ferromagnetic and electrical properties of Ce_7Rh_3 and Pr_7Rh_3 single crystals have been investigated by the measurements of magnetization, magnetic susceptibility, electrical resistivity and thermal expansion. As previously reported, the two compounds are ferromagnetic at low temperature. In the ferromagnetic state, Ce_7Rh_3 has a uniaxial magnetic anisotropy along the *c*-axis. On the contrary, Pr_7Rh_3 shows the relatively large in-plane magnetic anisotropy. Magnetic anisotropy energy estimated from the magnetization curves at 4.2 K is $K_{u1} = 6.32 \times 10^2$ erg/cm^3 for Ce_7Rh_3 and $K_{u2} = 1.90 \times 10^5$ erg/cm^3 for Pr_7Rh_3, respectively. Saturation magnetization at 4.2 K is 0.98 μ_B/Ce for Ce_7Rh_3 and 1.38 μ_B/Pr for Pr_7Rh_3 which are smaller than the gJ value of Ce^{3+} and Pr^{3+} free ions indicating the existence of crystal electric field (CEF) effect. Magnetic anisotropy axis of Ce_7Rh_3 is different from the prediction by the point charge model. This can be described by the 4f-conduction electron hybridization in the *c*-plane. Electrical resistivity of Ce_7Rh_3 indicates the existence of the Kondo scattering.

PACS: 72.15; 75.50

Keywords: Ce_7Rh_3; Pr_7Rh_3; Magnetic susceptibility; Magnetization; Electrical resistivity; Kondo effect; Magnetic anisotropy

1. Introduction

The rare earth intermetallic compounds R_7Rh_3 crystallize in the Th_7Fe_3 type hexagonal structure with space group $P6_3mc$ in which the R atom occupies three non-equivalent sites [1–3]. In this system, almost all the rare earth elements form R_7Rh_3 compounds with Rh. Magnetic and electrical properties have been reported by several authors [4–8]. Among them, La_7Rh_3 is a Pauli paramagnetic superconductor with the superconducting transition temperature of $T_S = 2.6$ K [4]. In the other compounds, Ce_7Rh_3 and Pr_7Rh_3 are ferromagnetic below $T_C = 6.8$ K and 14.1 K, respectively and show metallic electrical conduction [6,8]. On the other hand, the R_7Rh_3 (R = Gd and Tb to Er) compounds and Y_7Rh_3 show a negative temperature coefficient of the electrical resistivity in the high temperature region indicating the compensated semimetal or degenerated semiconductor [9]. Furthermore, Ce_7Rh_3 shows the heavy fermion characteristics [5–7]. Since these studies were carried out using polycrystalline samples, detailed properties of these compounds were not so clear. In the present study, we have succeeded to make single crystals of Ce_7Rh_3 and Pr_7Rh_3 and investigated the magnetic and electrical properties of these two compounds. In this report, we will present the experimental results of magnetic, electrical and thermal measurements and the detailed ferromagnetic behavior of Ce_7Rh_3 and Pr_7Rh_3 will be discussed.

2. Experimental

Polycrystalline samples of Ce_7Rh_3 and Pr_7Rh_3 were prepared by arc-melting the constituent elements of 99.9% Ce, Pr and 99.96% Rh under high purity argon atmosphere. Single crystals were obtained by a Czochralski method from single-phase polycrystalline samples using a tri-arc furnace. Rectangular and sphere samples were cut from the single crystalline ingots. The dimension of the *c*-axis sample of Ce_7Rh_3 is 2.0 mm × 1.8 mm × 4.9 mm; the other rectangular samples have almost the same dimensions. All the samples were annealed at 500 °C for 24 h in an evacuated quartz tube. Powder X-ray diffraction indicated that the samples were all single-phase with the Th_7Fe_3-type hexagonal structure. The crystal orientation was determined by the back reflection Laue method. Measurements of the AC magnetic susceptibility χ_{AC} were made using a standard Hartshorn bridge circuit. Frequency and amplitude of the AC magnetic field are 100 Hz and 12 Oe, respectively. Magnetization and magnetic susceptibility were measured using a vibrating sample magnetometer in the magnetic field up to 17 kOe and in the temperature range from 4.2 to 300 K. The electrical

* Corresponding author. Tel.: +81 82 424 7089; fax: +81 82 424 5241.
E-mail address: tsutaok@hiroshima-u.ac.jp (T. Tsutaoka).

0925-8388/$ – see front matter © 2006 Elsevier B.V. All rights reserved.
doi:10.1016/j.jallcom.2006.11.033

resistivity ρ and thermal expansion $\Delta L/L$ were measured by a conventional DC four-terminal method and a strain gauge method, respectively. In the electrical resistivity measurements, the applied electrical current was 10 mA and the measurement number was 10 per point.

3. Results and discussion

3.1. Ferromagnetic behavior of Ce_7Rh_3 single crystals

The magnetization M curves of Ce_7Rh_3 at 4.2 K are shown in Fig. 1 along the c-axis and in the c-plane. For this sample, the magnetization was measured by the extraction method using a superconducting magnet up to 90 kOe. No magnetic anisotropy was observed in the c-plane. The magnetization curve along the c-axis indicates a ferromagnetic character and M slightly increases with increasing magnetic field H, in higher magnetic fields up to 90 kOe. In the c-plane, the M initially shows the linear increases with increasing H and approach to the curve along the c-axis. This result shows that Ce_7Rh_3 has a uniaxial type magnetic anisotropy with the c-axis as the easy axis. The saturation magnetization value, which is estimated by the extrapolation of the M to $1/H = 0$, is 0.98 μ_B/Ce. This is about one-half of the theoretical value of Ce^{3+}, 2.14 μ_B. The origin of this small saturation magnetization can be attributed to the crystal electric field (CEF) effect or the effect of the non-magnetic Ce ions. Since Ce_7Rh_3 has tree non-equivalent crystallographic sites, magnetic moment of each site can be different. From the entropy change at T_C determined by the specific heat measurements, Trovarelli and Sereni suggested that only the Ce ion at the site1 contributes to the ferromagnetic property and the Ce_2 and Ce_3 ion contribute the Kondo effect and the valence fluctuation, respectively [7]. However, assuming that the two of the 14 Ce ions in the unit cell carry the magnetic moment, magnetization value must be 1/7 of the full moment of Ce^{3+}. Since the obtained saturation magnetization value, 0.98 μ_B/Ce, is larger than the expected value by this assumption, all Ce ions can carry the magnetic moment. Further, the crystal symmetry of the site2 is the same as the site3 and is different from the site1. Thus, the magnetic moment at the site1 can be different from that at site2 and site3.

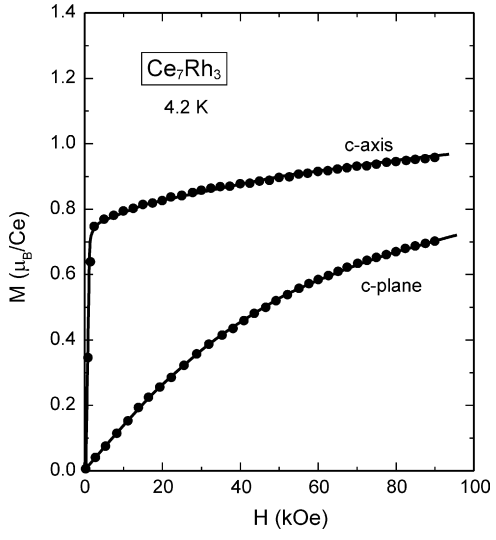

Fig. 1. Magnetization curves of Ce_7Rh_3 at 4.2 K.

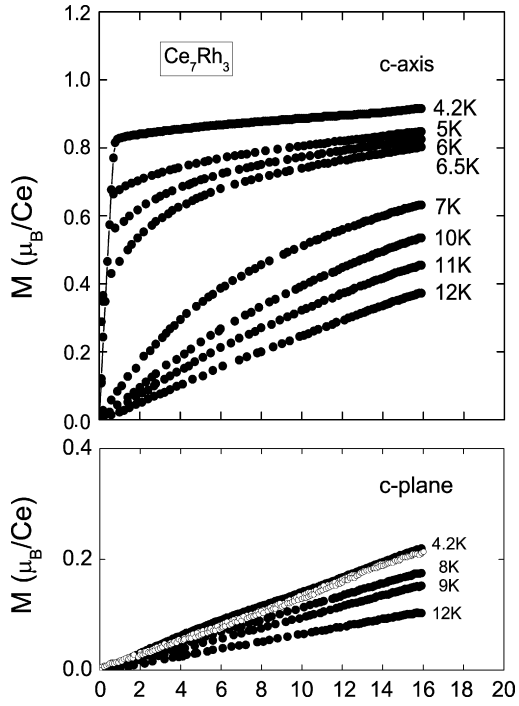

Fig. 2. Magnetization curves of Ce_7Rh_3 at various temperatures.

The temperature variation of the magnetization curve is shown in Fig. 2. Ferromagnetic property disappears between 6.5 and 7 K. The ferromagnetic Curie temperature T_C was determined to be 6.8 K from the χ_{AC} versus T data, displayed in Fig. 3. This value is in good agreement with the previously reported one [6,8]. A relatively large magnetic anisotropy is also observed in the χ_{AC} measurement. In the uniaxial magnetic anisotropy sys-

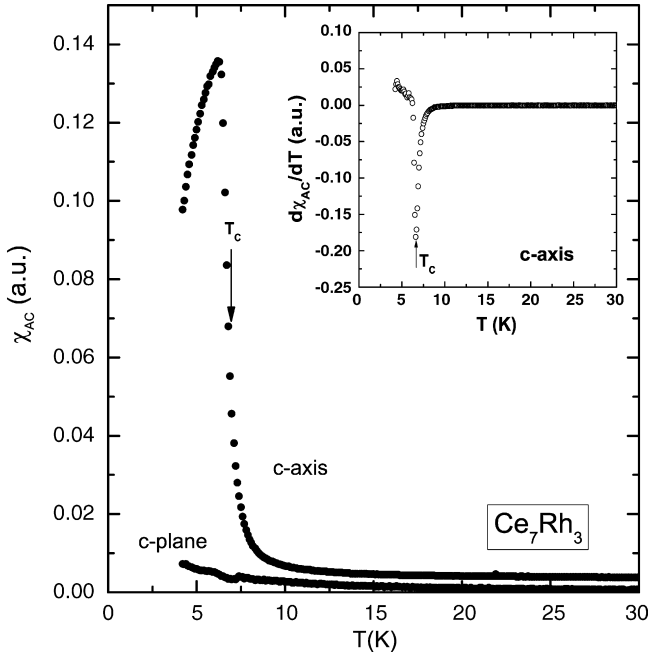

Fig. 3. AC magnetic susceptibility χ_{AC} of Ce_7Rh_3 as a function of temperature.

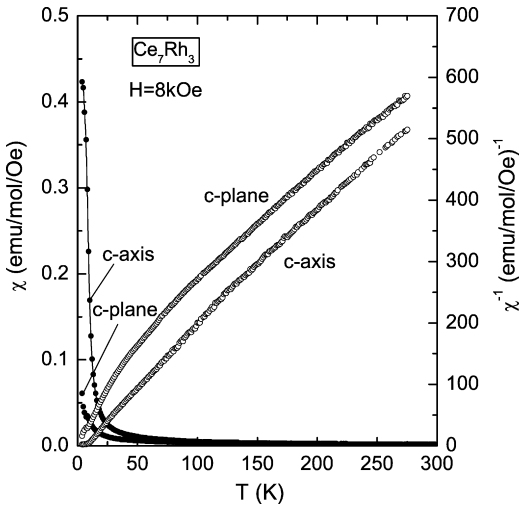

Fig. 4. Magnetic susceptibility χ and reciprocal susceptibility χ^{-1} of Ce_7Rh_3 as a function of temperature.

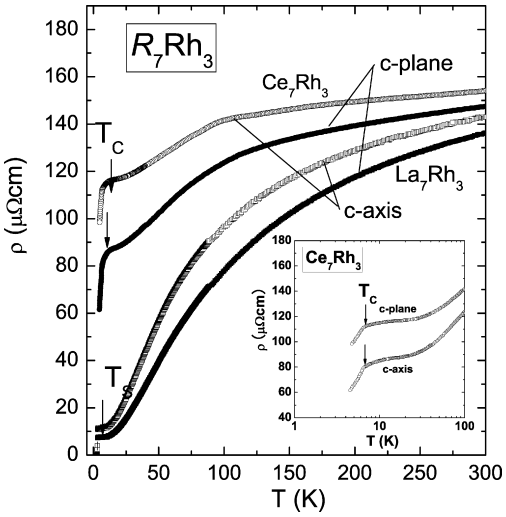

Fig. 5. Electrical resistivity ρ of Ce_7Rh_3 and La_7Rh_3 as a function of temperature. The inset is the low temperature part of ρ for Ce_7Rh_3.

tem with hexagonal structure, the hard axis magnetization can be described using two magnetic anisotropy constant K_{u1} and K_{u2} as follows [10],

$$4K_{u2}\frac{M^2}{M_S^4}+\frac{2K_{u1}}{M_S^2}=\frac{H_{eff}}{M}. \quad (1)$$

Here, M_S and H_{eff} are the saturation magnetization and the effective magnetic field, respectively. Effective magnetic field is represented by

$$H_{eff}=H-\frac{NM}{\mu_0}. \quad (2)$$

Here, N and μ_0 are the demagnetizing factor and the magnetic permeability of vacuum, respectively. From the intercept value of the H_{eff}/M versus M^2 curve, the magnetic anisotropy constant of Ce_7Rh_3 at 4.2 K was estimated. Obtained value is $K_{u1}=6.32\times10^2$ erg/cm^3. This obtained value is small compared to the value of hexagonal Co, $K_{u1}=6.86\times10^6$ erg/cm^3 at 4.2 K [11].

Fig. 4 shows the magnetic susceptibility χ and the reciprocal susceptibility χ^{-1} as a function of temperature. The magnetic susceptibility rapidly decreases with increasing temperature in both axes. Paramagnetic susceptibility above 50 K obeys the Curie–Weiss law. Effective magnetic moment μ_{eff}, which is obtained from the reciprocal susceptibility data, is 2.3 μ_B/Ce along the c-axis and 2.4 μ_B/Ce in the c-plane, respectively. These values have a good agreement to the theoretical value 2.54 μ_B of Ce^{3+}. The paramagnetic Curie temperature θ_p is 3.1 K for the c-axis and −53.6 K for the c-plane, respectively. From the molecular field theory, the CEF parameter $\boldsymbol{B}_2^0$ can be determined using θ_p values as follows [12],

$$\boldsymbol{B}_2^0=\frac{10(\theta_{p2}-\theta_{p1})}{3(2\boldsymbol{J}-1)(2\boldsymbol{J}+3)}, \quad (3)$$

where the θ_{p1} and θ_{p2} are the paramagnetic Curie temperature along the c-axis and in the c-plane, respectively and $\boldsymbol{J}$ is the total angular momentum of the rare earth ion. We obtained $\boldsymbol{B}_2^0=-5.91$ K for Ce_7Rh_3. We will discuss this negative value of $\boldsymbol{B}_2^0$ and the difference of the magnetic anisotropy axis between Ce_7Rh_3 and Pr_7Rh_3, later.

Fig. 5 shows the electrical resistivity ρ as a function of temperature T for a Ce_7Rh_3 single crystal. The inset shows the low temperature part. The electrical resistivity data of La_7Rh_3 are also shown in this figure [13]. In Ce_7Rh_3, the metallic electrical conduction was observed in both axes. The ρ of Ce_7Rh_3 slightly decreases with decreasing temperature from room temperature and shows a minimum at about 24 K and a rapid decrease at T_C. On the other hand, La_7Rh_3 shows the superconducting transition at $T_S=2.6$ K [4]. The minimum of ρ in Ce_7Rh_3 can be caused by the short range ferromagnetic ordering above T_C. It was reported that Ce_7Rh_3 shows the coexistence of ferromagnetic order and the Kondo effect [6,14]. To evaluate the Kondo scattering, the magnetic component of the electrical resistivity ρ_{mag} was estimated by subtracting the ρ of La_7Rh_3 from that of Ce_7Rh_3. The ρ_{mag} along the c-axis is shown in Fig. 6 as a

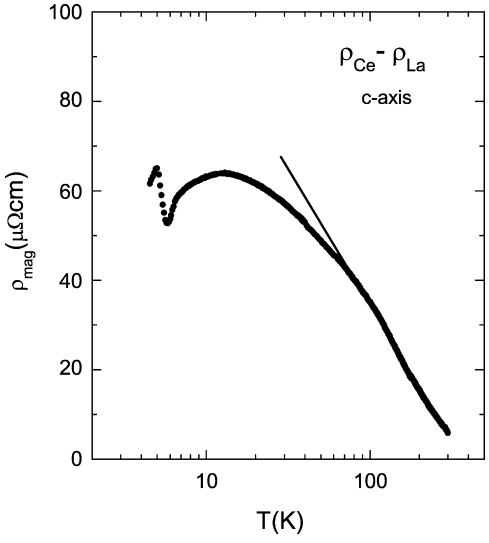

Fig. 6. Magnetic component of electrical resistivity ρ_{mag} of Ce_7Rh_3 along the c-axis as a function of temperature.

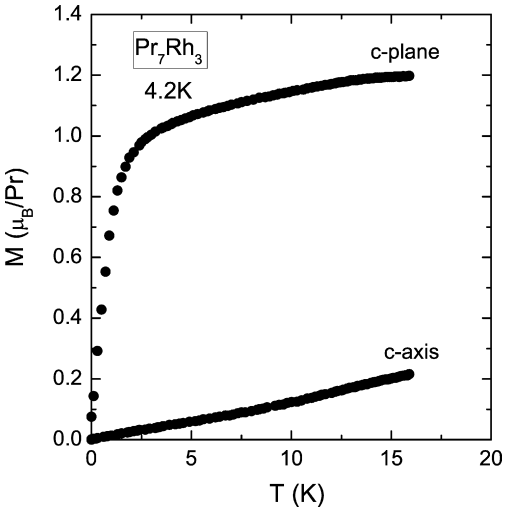

Fig. 7. Magnetization curves of Pr_7Rh_3 at 4.2 K.

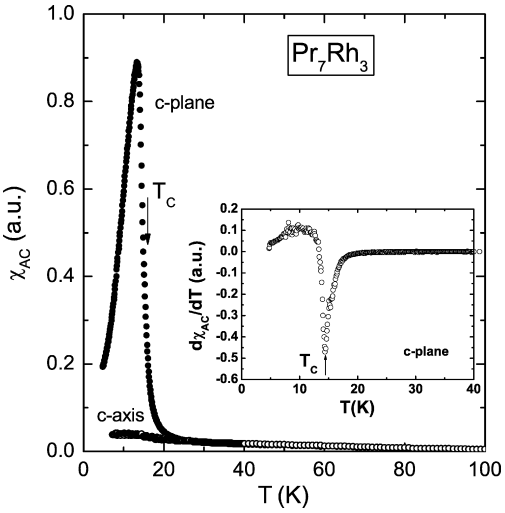

Fig. 9. AC magnetic susceptibility χ_{AC} of Pr_7Rh_3 as a function of temperature. The inset shows the $d\chi_{AC}/dT$ vs. T curve in the c-plane.

function of temperature. The high temperature variation of ρ_{mag} above 70 K shows a $-\log T$ dependence indicating the Kondo effect.

3.2. Ferromagnetic behavior of Pr_7Rh_3 single crystals

Magnetization M curves of Pr_7Rh_3 along the c-axis and in the c-plane at 4.2 K are shown in Fig. 7. These curves indicate that Pr_7Rh_3 has an easy-plane type magnetic anisotropy in the c-plane. The saturation magnetization value, which is estimated by the extrapolation of the M to $1/H = 0$, is 1.38 μ_B/Ce. This is about 40% of the theoretical value of Pr^{3+}ion in the ordered state ($\mu_{gJ} = 3.2\,\mu_B$). As temperature increases, magnetization curve along the c-plane becomes paramagnetic near 16 K as shown in Fig. 8(a). The M^2 versus H/M plot, i.e. Arrot plot, which is shown in Fig. 8(b) indicates that the Curie temperature T_C exists between 14 and 16 K. On the other hand, the gradient of the linear magnetization curve decreases with increasing temperature.

The AC magnetic susceptibility χ_{AC} is shown in Fig. 9 as a function of temperature T. The inset shows the $d\chi_{AC}/dT$ versus T curve in the c-plane. The Curie temperature T_C was determined to be 14.1 K from the inflection point of the temperature in the c-plane susceptibility (the inset of Fig. 9). A large magnetic anisotropy was also observed between the c-axis and the c-plane in the χ_{AC} curve. In the in-plane magnetic anisotropy system with hexagonal structure, the hard axis magnetization can be described as follows [10,15],

$$4K_{u2}\frac{M^2}{M_S^4} - \frac{2(K_{u1}+2K_{u2})}{M_S^2} = \frac{H_{eff}}{M}. \quad (4)$$

From the gradient of the H_{eff}/M versus M^2 curve, magnetic anisotropy constant of Pr_7Rh_3 at 4.2 K was estimated to be

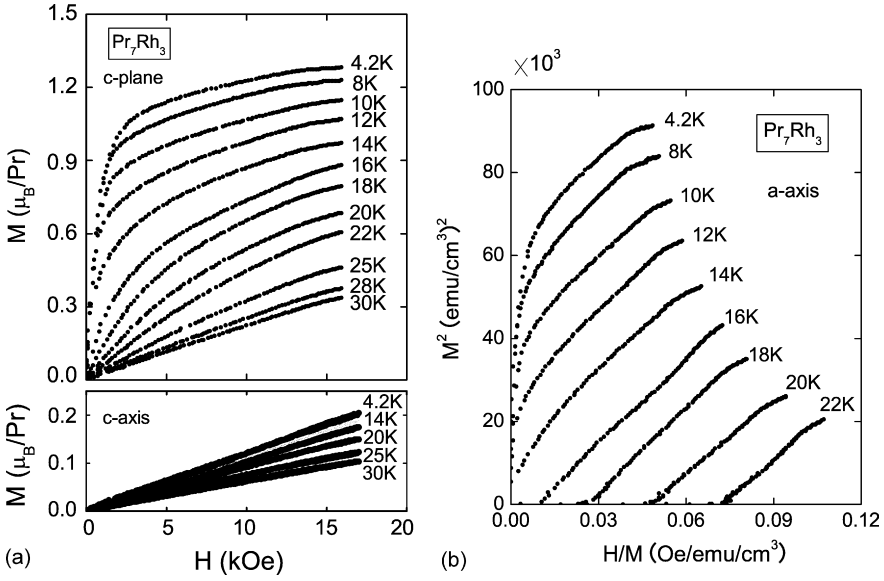

Fig. 8. Magnetization curves (a) and the Arrot plot (b) for Ce_7Rh_3 at several temperatures.

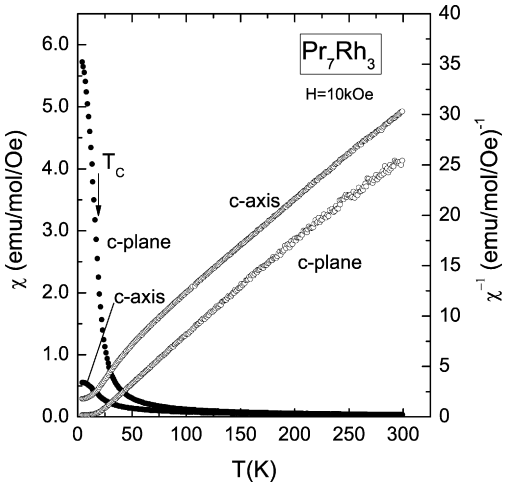

Fig. 10. Magnetic susceptibility χ and reciprocal susceptibility χ^{-1} of Pr_7Rh_3 as a function of temperature.

$K_{u2} = 1.90 \times 10^5$ erg/cm^3. This value is much larger than that of Ce_7Rh_3.

Magnetic susceptibility χ and reciprocal susceptibility χ^{-1} under 10 kOe along the c-axis and in the c-plane are shown in Fig. 10 as a function of temperature. The χ rapidly decreases with increasing temperature for both axes. The χ^{-1} curves indicates the linear temperature variation above 50 K indicating the Curie–Weiss law. Effective magnetic moment μ_{eff} determined from the paramagnetic susceptibility is 3.5 μ_B/Pr along the c-axis and 3.6 μ_B/Pr in the c-plane, respectively. These values have a good agreement to the theoretical value 3.58 μ_B of Pr^{3+}. Further, the paramagnetic Curie temperature, θ_p is −31.7 K for the c-axis and 8.6 K for the c-plane, respectively. The second order CEF parameter $\boldsymbol{B}_2^0$ determined by Eq. (3) is 1.74 K for Pr_7Rh_3.

Fig. 11 shows the electrical resistivity ρ as a function of temperature T for a Pr_7Rh_3 single crystal. The inset shows the low temperature parts. Pr_7Rh_3 also shows the metallic conduction and the ρ decreases with decreasing temperature and shows a

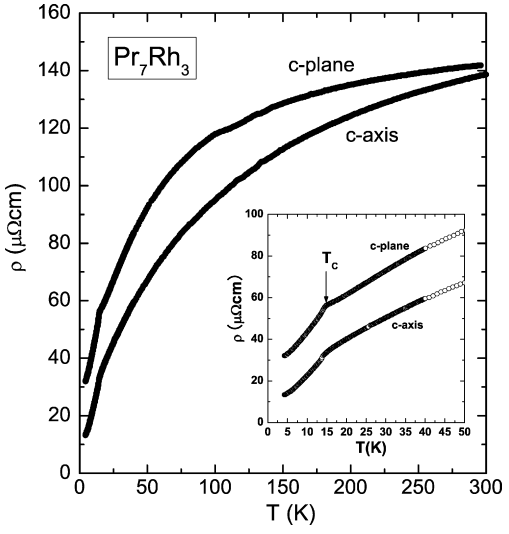

Fig. 11. Electrical resistivity ρ of Pr_7Rh_3 as a function of temperature. The inset shows the low temperature part of ρ for Pr_7Rh_3.

kink at T_C. The electrical resistivity in the paramagnetic state shows the negative curvature in both axes; temperature dependence of ρ does not follow the Bloch–Grüneisen equation. This behavior could be originated by the s–d interband scattering which was described by Mott and Jones [16]. This behavior is also seen in La_7Rh_3 as shown in Fig. 5.

3.3. The magnetic anisotropy difference between Ce_7Rh_3 and Pr_7Rh_3

We consider the CEF parameter $\boldsymbol{B}_2^0$ of Ce_7Rh_3 and Pr_7Rh_3. From the point charge model, the $\boldsymbol{B}_2^0$ can be estimated using the following equation [17],

$$\boldsymbol{B}_2^0 = \alpha_J \langle r^2 \rangle (1-\sigma) A_2^0 = -\alpha_J \langle r^2 \rangle (1-\sigma) \times \sum_i \left(\frac{5}{\pi}\right)^{1/2} \frac{Z_i e^2}{R_i^3} (3\cos^2\theta_i - 1) \quad (5)$$

where α_J is the Stevens factor and $\langle r^2 \rangle$ is the mean square of the radial wave function of 4f electrons. This value was calculated by Freeman and Watson [18]. The σ is a shielding factor; we assume this 0.5. The Z_i is the valence of the ion and the R_i is the distance between the origin and the position of the ith atom. The θ_i is the angle from the quantized axis. Assuming that the valence of R and Rh is 3+ and 1+, respectively, $\boldsymbol{B}_2^0$ was calculated using the atoms included in the nearest neighbor polyhedron. Obtained value of $\boldsymbol{B}_2^0$ is 13.16 K for Ce_7Rh_3 and 3.86 K for Pr_7Rh_3, respectively. Comparing the $\boldsymbol{B}_2^0$ value from the magnetic susceptibility data, −5.91 K for Ce_7Rh_3 and 1.74 K for Pr_7Rh_3, to the calculated ones, a reasonable agreement was obtained in Pr_7Rh_3. However, in Ce_7Rh_3, the experimentally obtained $\boldsymbol{B}_2^0$ value has the opposite sign and shows a large difference from the expected one by the point charge model. Generally, the magnetic anisotropy axis is determined by the interaction between the ligand and the 4f electrons in the rare earth compounds; the distribution of the 4f electrons can be reflected on the sign of the Stevens factor in Eq. (5). It is known that the Stevens factor is negative for Ce, Pr, Nd, Tb, Dy and Ho. Thus, the sign of $\boldsymbol{B}_2^0$ must be positive and the in-plane magnetic anisotropy can be maintained in Ce_7Rh_3 and Pr_7Rh_3. We discuss this discrepancy of the anisotropy axis in Ce_7Rh_3 considering the distribution of the 4f electrons on the three rare earth sites R1, R2 and R3.

In the R_7Rh_3 system, the lattice constant of the c-axis is smaller than that of the a-axis. From this geometry, at the R1 and R3 sites, the number of R^{3+} ions situated along the c-axis is larger than that in the c-plane. Thus, the 4f electrons at R1 and R3 tend to be distributed along the c-axis; the magnetic moments can be polarized in the c-plane as shown in Fig. 12. On the other hand, the 4f electrons at R2 site are distributed in the c-plane due to the distribution of the other R^{3+} ions around it; magnetic moments are polarized along the c-axis. Since there are four R1 and R2 sites and three R2 sites in R_7Rh_3, the total 4f electron distribution can be stabilized along the c-axis. In Pr_7Rh_3, the in-plane magnetic anisotropy is considered to be achieved by this mechanism. On the other hand, it is known that the 4f electron hybridizes with the conduction electron in Ce compounds.

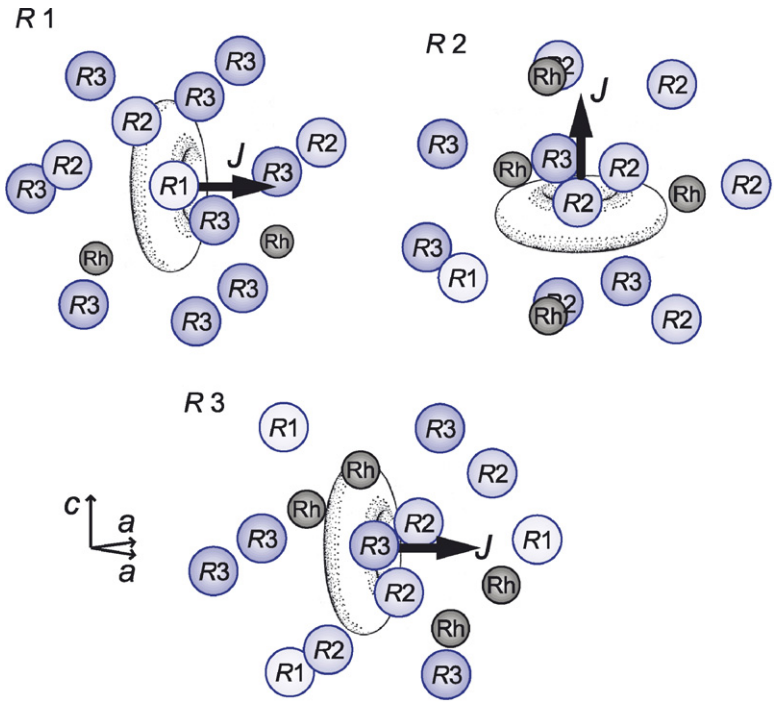

Fig. 12. Schematic diagram of the distribution of 4f electron around the each rare earth site in R_7Rh_3.

Thus the strong 4f-conduction electron hybridization in the *c*-plane makes the 4f electrons distribution in the *c*-plane; magnetic moments are polarized along the *c*-axis in Ce_7Rh_3. And this can bring about the uniaxial magnetic anisotropy in Ce_7Rh_3.

The thermal expansion of Ce_7Rh_3 can be also explained by the hybridization effect. Fig. 13 shows the thermal expansion $\Delta L/L$ of a Ce_7Rh_3 single crystal. With decreasing temperature, the $\Delta L/L$ decreases in the *c*-plane and increases along the *c*-axis. Since the lattice shrinkage in the *c*-plane is caused by the 4f-cnduction electron hybridization; the lattice expands to the *c*-axis to compensate the lattice energy. Such kind of the change in the magnetic anisotropy axis was also found in Ce_7Ni_3 [19,20].

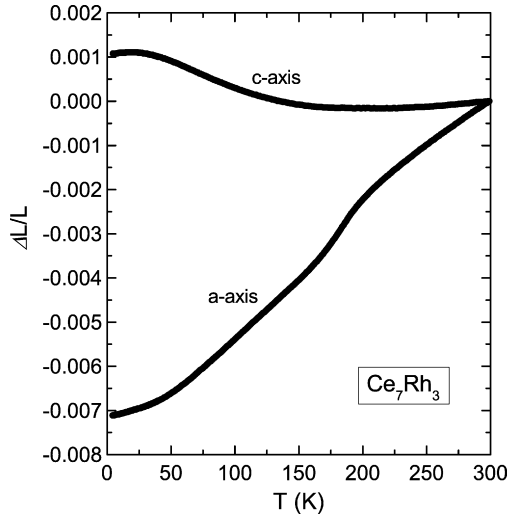

Fig. 13. Thermal expansion $\Delta L/L$ of Ce_7Rh_3 as a function of temperature.

The origin of the small magnetic anisotropy in Ce_7Rh_3 compared to that in Pr_7Rh_3 can be realized from this hybridization effect.

4. Conclusions

Ferromagnetic properties of Ce_7Rh_3 and Pr_7Rh_3 single crystals have been investigated. Ce_7Rh_3 has uniaxial magnetic anisotropy along the *c*-axis; on the contrary, Pr_7Rh_3 has in-plane anisotropy in the basal plane. The magnetic anisotropy energy has been estimated for these compounds at 4.2 K. The uniaxial magnetic anisotropy in Ce_7Rh_3 can be realized by the 4f-conduction electron hybridization. In Ce_7Rh_3, the coexistence of the Kondo effect and ferromagnetic order was observed. The CEF parameter $\boldsymbol{B}_2^0$ was experimentally examined from the magnetic susceptibility data and was also calculated by the point charge model. Reasonable agreement in $\boldsymbol{B}_2^0$ value was obtained in Pr_7Rh_3.

References

[1] A. Raman, J. Less-Common Met. 26 (1972) 199.
[2] R.B. Loof Jr., A.C. Larson, D.T. Cromer, Acta Cryst. 14 (1961) 1084.
[3] G.L. Olcese, J. Less-Common Met. 33 (1973) 71.
[4] P. Pedrazzini, G. Schmerber, M.G. Berisso, J.P. Kappler, J.G. Sereni, Physica C 336 (2000) 10.
[5] J.G. Sereni, O. Trovarelli, G. Schmerber, J.P. Kappler, J. Magn. Magn. Mater. 108 (1992) 183.
[6] O. Trovarelli, J.G. Sereni, G. Schmerber, J.P. Kappler, Physica B 206 & 207 (1995) 243.
[7] O. Trovarelli, J.G. Sereni, J. Low Temp. Phys. 108 (1997) 53.
[8] T. Tsutaoka, Y. Nakamori, T. Tokunaga, H. Kadomatsu, Y. Itoh, J. Alloys Compd. 270 (1998) 53.

[9] T. Tsutaoka, Y. Nakamori, T. Tokunaga, Y. Itoh, J. Phys. Soc. Jpn. 70 (2001) 199.
[10] W. Sucksmith, J.E. Thompson, Proc. R. Soc. 225 (1954) 362.
[11] R. Pauthenet, Y. Barnier, G. Rimet, J. Phys. Soc. Jpn. 17 (Suppl. B–I) (1962) 309.
[12] G.J. Bowden, D.St.P. Bunbury, M.A.H. McCausland, J. Phys. C 4 (1971) 1840.
[13] Y. Nakamori, H. Fujii, T. Tsutaoka, T. Tokunaga, M. Ito, T. Suzuki, T. Fujita, Physica B 329–333 (2003) 1087.
[14] T. Tsutaoka, M. Takahashi, T. Tokunaga, Y. Nakamori, Acta Phys. Pol. B 34 (2003) 1355.
[15] H.P. Klein, A. Menth, R.S. Perkins, Physica B 80 (1975) 153.
[16] N.F. Mott, F. Jones, The Theory of the Properties of Metals and Alloys, Oxford University Press, London, 1936, p. 268.
[17] M.T. Hutchings, Solid State Phys. 16 (1964) 227.
[18] A.J. Freeman, R.E. Watson, Phys. Rev. 127 (1962) 2058.
[19] D. Ginoux, J.C. Gomez-Sal, J. Appl. Phys. 57 (1985) 3125.
[20] K. Umeo, K. Ishii, H. Kadomatsu, Solid State Commun. 90 (1994) 321.